

ORIGINAL RESEARCH

Open Access



# A semi-automatic technique to quantify complex tuberculous lung lesions on $^{18}\text{F}$ -fluorodeoxyglucose positron emission tomography/computerised tomography images

Stephanus T. Malherbe<sup>1,2\*</sup> , Patrick Dupont<sup>3,4</sup>, Ilse Kant<sup>4</sup>, Petri Ahlers<sup>1,2</sup>, Magdalena Kriel<sup>1,2</sup>, André G. Loxton<sup>1,2</sup>, Ray Y. Chen<sup>5</sup>, Laura E. Via<sup>5,6</sup>, Friedrich Thienemann<sup>6,7</sup>, Robert J. Wilkinson<sup>6,7,8,9</sup>, Clifton E. Barry III<sup>1,2,5,6</sup>, Stephanie Griffith-Richards<sup>10</sup>, Annare Ellman<sup>4</sup>, Katharina Ronacher<sup>1,2,11</sup>, Jill Winter<sup>1,2</sup>, Gerhard Walzl<sup>1,2</sup>, James M. Warwick<sup>4</sup> and the Catalysis Biomarker Consortium

## Abstract

**Background:** There is a growing interest in the use of  $^{18}\text{F}$ -FDG PET-CT to monitor tuberculosis (TB) treatment response. However, TB causes complex and widespread pathology, which is challenging to segment and quantify in a reproducible manner.

To address this, we developed a technique to standardise uptake (Z-score), segment and quantify tuberculous lung lesions on PET and CT concurrently, in order to track changes over time. We used open source tools and created a MATLAB script. The technique was optimised on a training set of five pulmonary tuberculosis (PTB) cases after standard TB therapy and 15 control patients with lesion-free lungs.

**Results:** We compared the proposed method to a fixed threshold ( $\text{SUV} > 1$ ) and manual segmentation by two readers and piloted the technique successfully on scans of five control patients and five PTB cases (four cured and one failed treatment case), at diagnosis and after 1 and 6 months of treatment. There was a better correlation between the Z-score-based segmentation and manual segmentation than  $\text{SUV} > 1$  and manual segmentation in terms of overall spatial overlap (measured in Dice similarity coefficient) and specificity (1 minus false positive volume fraction). However,  $\text{SUV} > 1$  segmentation appeared more sensitive. Both the Z-score and  $\text{SUV} > 1$  showed very low variability when measuring change over time. In addition, total glycolytic activity, calculated using segmentation by Z-score and lesion-to-background ratio, correlated well with traditional total glycolytic activity calculations. The technique quantified various PET and CT parameters, including the total glycolytic activity index, metabolic lesion volume, lesion volumes at different CT densities and combined PET and CT parameters. The quantified metrics showed a marked decrease in the cured cases, with changes already apparent at month one, but remained largely unchanged in the failed treatment case.

(Continued on next page)

\* Correspondence: [malherbe@sun.ac.za](mailto:malherbe@sun.ac.za)

<sup>1</sup>DDST-NRF Centre of Excellence for Biomedical Tuberculosis Research and South African Medical Research Council Centre for Tuberculosis Research, Cape Town, South Africa

<sup>2</sup>Division of Molecular Biology and Human Genetics, Faculty of Medicine and Health Sciences, Stellenbosch University, Cape Town, South Africa

Full list of author information is available at the end of the article

(Continued from previous page)

**Conclusions:** Our technique is promising to segment and quantify the lung scans of pulmonary tuberculosis patients in a semi-automatic manner, appropriate for measuring treatment response. Further validation is required in larger cohorts.

**Keywords:**  $^{18}\text{F}$ -fluorodeoxyglucose (FDG) positron emission tomography (PET)/computed tomography, Tuberculosis, Image analysis, Lesion segmentation, Lesion quantification

## Background

Positron emission tomography/computerised tomography (PET-CT) is well established in the diagnostic workup, treatment planning and response assessment of cancer and various inflammatory and infectious diseases [1, 2]. The most commonly used PET tracer is  $^{18}\text{F}$ -fluorodeoxyglucose (FDG). It reflects glucose metabolism and shows increased uptake in areas of inflammation. PET scanners measure the radiopharmaceutical concentration in tissue [3–5].

Uptake intensity in tissue is variable and influenced by numerous patient-, timing- and equipment factors, which is why the lesion-to-background ratio is often considered a more robust measure than absolute uptake [6]. Several semi-quantitative measurements of PET voxel intensity have been developed, of which standardised uptake value (SUV), is most commonly used. It compensates for variation in body size, injected activity and radioactive decay.

The metabolic lesion volume (MLV), maximum and mean SUV within the lesion ( $\text{SUV}_{\text{max}}$  and  $\text{SUV}_{\text{mean}}$ ) and the total glycolytic activity ( $\text{TGA} = \text{MLV} \times \text{SUV}_{\text{mean}}$ ) are the PET parameters most commonly used for lesion quantification [3, 4, 7–9].

The borders of the MLV can be delineated visually or using various semi-automated techniques, however no single technique has proven optimal for all applications [6]. In most cases lesion delineation is still performed manually, based on visual interpretation of PET or CT images. This is prone to inter- and intra-operator variation, especially for PET due to its lower spatial resolution and inherent noise [8–15]. Multiple methods are used and proposed to decrease variation in lesion segmentation. These include using reference values to normalise the lesion- to- background uptake intensity by comparison to liver or mediastinal blood pool uptake [16–18] and the use of automated segmentation techniques. Automated segmentation techniques include thresholding techniques, gradient-based techniques and stochastic- and learning-based computerised methods [6]. Thresholds may be fixed or adaptive. Adaptive thresholds utilises image parameters, such as lesion-to-background ratio, mean background intensity and estimated lesion intensity in algorithms to define the threshold.

Some studies also focused on the quantification of images from CT scanners, which measure the density of

anatomical structures and lesions in Hounsfield units (HU). It is not a functional scan and is less prone to interscan variability. Only a few studies have evaluated densometric quantification of CT scans in diffuse lung disease; however, it appears to be reproducible and correlate well with other disease markers [19–22]. Joint segmentation of fused PET and CT images has shown improved robustness compared to methods using only data from PET [23].

The shortcomings of sputum culture to accurately indicate when TB treatment has achieved sterilising cure [24–26] escalate the cost to develop improved TB treatment options. This has led to a growing interest to use PET-CT imaging to monitor TB treatment response [27–29]. In animal models, FDG PET-CT has been used to accurately describe disease progression and response to treatment in pulmonary tuberculosis (PTB) [30–35]. Human studies have also shown PET-CT of promise to monitor the effect of treatment using simple descriptive techniques [27, 31, 36–41]. We recently reported PET-CT findings in PTB patients, before, during and after therapy, and found strikingly complex and heterogeneous lesion responses [42].

Reproducible segmentation and quantification becomes particularly important in diseases with heterogeneous morphology, vague borders and multi-focal distribution throughout an organ or system, such as TB or sarcoidosis [31, 41] (example shown in Fig. 1). This is especially important when accurate tracking of changes over time is required. In most animal model PET-CT studies, the authors used manual lesion delineation to track changes throughout the lungs, or in individual lesions [30–35]. Two separate human studies implemented whole lung quantification of PET (using fixed thresholds of  $\text{SUV} > 1$  and  $\text{SUV} > 2$ , respectively) and semi-quantitative CT reader scores [31, 41]. These found that quantified PET images were more robust than reader-based CT scores, and seemed to accurately measure changes in disease burden over time. To account for the spatially complex lesions, two studies successfully utilised computer-aided segmentation, respectively, based on affinity propagation and both interactive region growing and adaptive thresholding, in PET images of TB-infected small animal models [43, 44].

In this report, we describe a semi-automated, voxel-based technique developed for both PET and CT



**Fig. 1** 3D rendered anterior view of fused <sup>18</sup>F-FDG-PET-CT scan, performed at diagnosis on a patient with sputum culture positive pulmonary tuberculosis. It shows a wide distribution of lesions with complex morphology, including a large cavity in the left upper lobe with surrounding nodular infiltrates and patches of consolidation in the left lower lobe

quantification to standardise and segment widespread and heterogenous lesions throughout the lung and reproducibly measure disease burden over time.

**Methods**

**Study design**

The method was optimised on a training set of 15 lesion-free lung scans obtained from patients undergoing PET-CT scans for non-pulmonary clinical indications, as well as scans from five PTB patients showing residual lung lesions after treatment.

As a proof of concept, we applied the methodology to quantify disease burden on an independent test set of PET-CT scans from five controls and serial scans from the first five patients participating in the PTB cohort study, mentioned above [42]. The controls were from

the same communities (Cape Town, South-Africa), and had contact with PTB patients, but were sputum culture negative for *Mycobacterium tuberculosis* and had no active lesions visible on PET-CT scan. PTB cases were all diagnosed with drug-sensitive TB strains and were HIV negative. Cases underwent scans at time-points within 1 week from initiation of treatment (Dx), after 1 month of treatment (M1) and after 6 months of treatment (M6), corresponding with the duration of standard TB therapy. At the end of treatment, four of the PTB cases were sputum culture negative and classified as cured by healthcare providers in charge of treatment, while one was still sputum culture positive and diagnosed as a failed treatment outcome. The study design is summarised in Table 1.

**PET-CT imaging**

PET-CT scanning was performed with a Philips Gemini Big Bore time-of-flight scanner according to internationally accepted guidelines [45]. Patients fasted for 6 h before FDG administration, but were encouraged to hydrate well. According to body weight, participants received 185–259 MBq of <sup>18</sup>F-FDG intravenously 60 min before scan acquisition. PET images were reconstructed to 4 × 4 × 4 mm voxels using an iterative algorithm including time-of-flight information and corrections for random events, scatter, deadtime, attenuation and decay. The CT scan parameters were set at 120 kV, 100 mAs, without dose modulation with 1.17 × 1.17 mm pixels and a 3 mm slice thickness.

**Pre-processing**

We exported images from the PET-CT workstation in DICOM format and converted to ANALYSE file format [46] using MRIConvert [47]. To ensure reproducibility and facilitate direct comparison, we co-registered each patient’s follow-up scans with the baseline CT, using Statistical Parametric Mapping (SPM8) [48] with MATLAB 2013b (Mathworks Inc.). During the

**Table 1** Study design for method development and pilot application

Group	Training set		Test set	
	Negative controls	Positive controls	Negative controls	PTB cases
	n = 15	n = 5	n = 5	n = 5
PET-CT indication	Clinical	Observational cohort	Observational cohort	Observational cohort
Clinical background	Diagnostic work-up	PTB patients, after treatment	PTB contacts	PTB patients on treatment,
Scan time-points	Single scan	Single scan, after TB treatment	Single scan	Baseline, month 1 and month 6 of treatment
Lung scan findings	Lesion free	Minimal to mild intensity lesions after TB treatment	Lesion free	Extensive lesions
Main function of inclusion	Optimising Z-score threshold specificity	Optimising Z-score threshold sensitivity	Testing specificity	Pilot application

co-registration (using within-subject rigid-body model), CT images were re-sliced to the voxel matrix of the corresponding PET scan (using trilinear interpolation). This allowed direct voxel-based comparison of each patient's PET and CT images.

### Lung masks for PET and CT

For each series of co-registered CT studies, we generated a volume of interest (VOI) as a lung mask (Fig. 2a), in MRICro version 1.39 [49] on overlaid CT images, using the 3D region-growing, gradient-based tool. This allowed setting the origin, radius and difference from

origin and edge gradient on the overlaid CT images. We combined this with manual corrections, to avoid the exclusion of dense lesions extending into the pleura from the VOI. The lung mask excluded the lung hila and main pulmonary vessels, but included smaller vessels. As a final adjustment, we created a VOI of organs around the lungs that included in the lung fields by misregistration [usually the liver, spleen and mediastinum (Fig. 2b)], with the region-growing tool on the PET scans, and then deleted overlapping voxels from the lung mask. We converted the mask to a binary image and filled any holes in the mask, using ImageJ software [50] (Fig. 2c).

### PET quantification: background reference

We selected two areas of normal lung parenchyma (NL) as a reference VOI to standardise uptake in lung voxels (Fig. 2d) [50]. Each NL volume consisted of spheres 15 to 25 mm in diameter that visually appeared lesion-free on all co-registered scans. To enhance the representivity of the sample, the spheres were selected in opposite lungs or in some cases in different ipsilateral lobes, depending on the distribution of lung pathology.

### PET image quantification

We then quantified the pre-processed series of PET-CT images, using a MATLAB script developed in-house. The script quantified disease burden from the PET images by assigning a Z-score to all voxel counts within the lung mask based on the equation below:

$$Z = \frac{\text{counts} - \mu_{NL}}{\sigma_{NL}}$$

in which  $\mu_{NL}$  and  $\sigma_{NL}$  are the mean and standard deviation of PET counts within the normal volume for each study.

The Z-score provided a statistical way to standardise relative intensity of FDG uptake throughout the lungs. All lung voxels exceeding a defined Z-score threshold were defined as part of FDG-avid lesions. We then exported images of segmented lesion volumes to view alongside the original images for visual quality assessment.

To determine the optimal Z-score threshold, we processed a set of 15 lesion-free lung scans with reiterations of increasing Z-score thresholds, to minimise false positive findings. As expected, at a low Z-score threshold, the volumes segmented as abnormal in these healthy lungs were high, but decreased to a value close to zero for  $Z \geq 8$  (Fig. 3). To minimise false negative findings, we also tested increasing Z-score thresholds on scans that showed residual lesions with minimal or mild intensity and complex morphology, obtained from five PTB patients after treatment. Intensity was graded using an adaptation of the Deauville classification [18, 42]. A threshold of  $Z = 8$  delineated all lesions with minimal FDG avidity, while  $Z = 9$

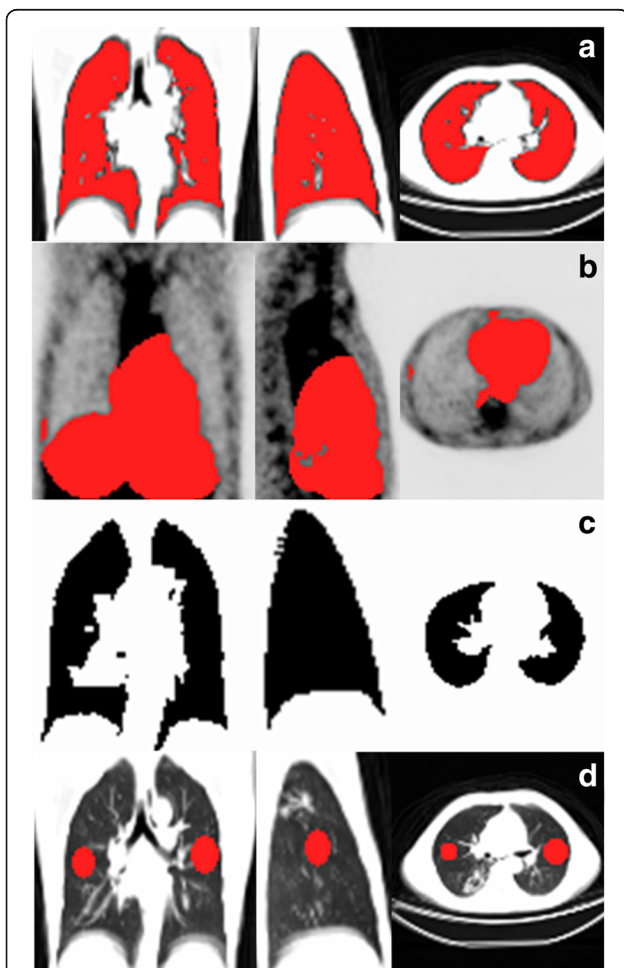


**Fig. 2** Example of volumes of interest (in red) required for quantification. **a** Lung mask, on the combined CT images from baseline and follow-up scans. **b** Volume of structures surrounding the lung affecting motion misregistration (usually the mediastinum, liver and spleen) drawn on the overlaid PET images. We then deleted overlapping areas on the lung mask to leave only areas unaffected by misregistration. **c** Binary image representing the final lung mask. **d** Reference volumes of normal lung tissue, represented by two spheres in opposite lungs or ipsilateral lobes. It is also drawn on the overlaid CT images, but viewed alongside the PET images to ensure that it represents lesion-free lung

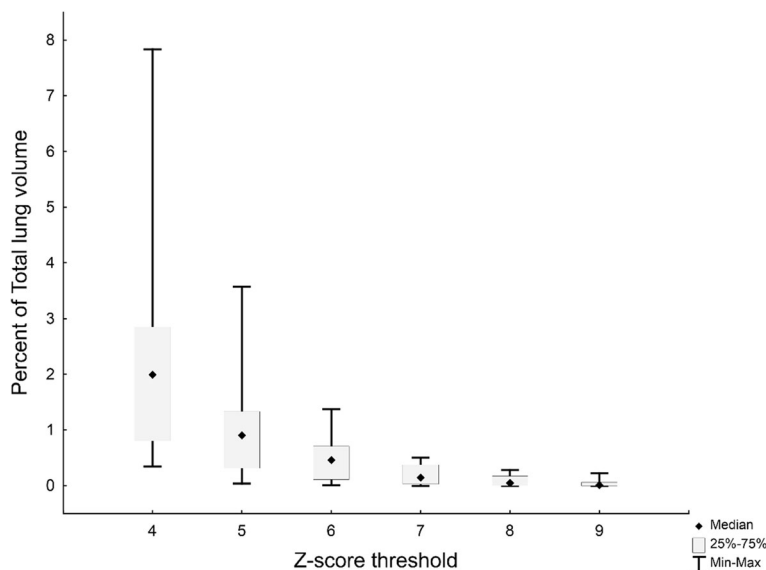


**Fig. 3** The range, median and 25th and 75th percentiles for percentage of total lung volume classified as FDG avid at different Z-score thresholds [4–9], in the quantification of PET-CT scans from 15 controls with visually lesion-free lungs

delineated all lesions with mild FDG avidity, but failed to detect some lesions with minimal FDG avidity (Fig. 4). We thus chose a cut-off of  $Z = 8$  based on its low false positive and false negative rates.

For comparison, two readers manually delineated FDG-avid lung lesions of diagnosis (Dx) and M6 scans, based on visual assessment. We also applied different thresholds for automated segmentation within the lung mask, namely  $SUV > 1$  and T40%.  $SUV > 1$  is a fixed threshold, used in previous TB studies [41] to delineate lung lesions on PET, while T40% refers to 40% of the maximum intensity in a VOI, previously used in cancer studies [6].

**CT density quantification**

Concurrently with the PET segmentation and using the same lung mask, the MATLAB script also segmented the CT images into five categories based on the density of each voxel compared to set values obtained from literature [21, 41]: (1) low density ( $< -950$  HU), attributed to cavitation or extremely hyper-inflated lung tissue ( $V_{low}$ ); (2) normal density, between  $-950$  HU and  $-500$  HU; (3) soft lesion volume ( $V_{soft}$ ), from  $-500$  HU to  $-300$  HU, usually tree-in-bud lesions or nodules, but may also include regular, medium to large vasculature; and (4) medium lesion volume ( $V_{medium}$ ) from  $-300$  HU to  $-100$  HU. This category should include very little normal lung tissue and usually consists of nodular infiltrates, but may also include hard lesions in early progression or partial resolution; (5) hard lesion volume ( $V_{hard}$ ), above  $-100$  HU, are usually due to consolidation, cavity walls, bronchial thickening or calcified fibrosis.

We performed visual checks of the accuracy of CT lesion delineation, based on these fixed density thresholds. For lesions with increased density ( $V_{soft}$ ,  $V_{medium}$ ,  $V_{hard}$ ), the segmented areas corresponded well to lesion morphology. However, using  $-950$  HU as the upper limit for low-density lesions was not specific enough for cavitation and the segmented areas in some cases included bullae, bronchiectasis, and severe emphysema. This necessitated an additional step to measure the volumes of individual cavities for each scan. This was done using the MRICro’s 3D region-growing tool (boundary-based segmentation).

**PET lesion intensity quantification**

After segmentation, the program quantified the following PET parameters: (1) MLV, (2) the mean Z-score in the MLV ( $Z_{mean}$ ), (3) TGA ( $MLV \times SUV_{mean}$ ), (4) total glycolytic activity index (TGAI): the product of the MLV and mean lesion-to-background intensity ( $TGAI = MLV \times mean\ lesion\ counts / mean\ counts\ in\ normal\ lung$ ). In addition, the program also measured the total lung volume [TLV (ml)] and the volumes of each abnormal density category on CT, i.e.,  $V_{low}$ ,  $V_{soft}$ ,  $V_{medium}$ , and  $V_{hard}$ , as well as a combined PET-CT metric:  $MLV_{abN}$  [the intersection of MLV and area with increased density on CT ( $\geq 500$  HU)].

Re-slicing of the CT to the corresponding PET allowed the program to compare CT density and PET intensity, directly per voxel.

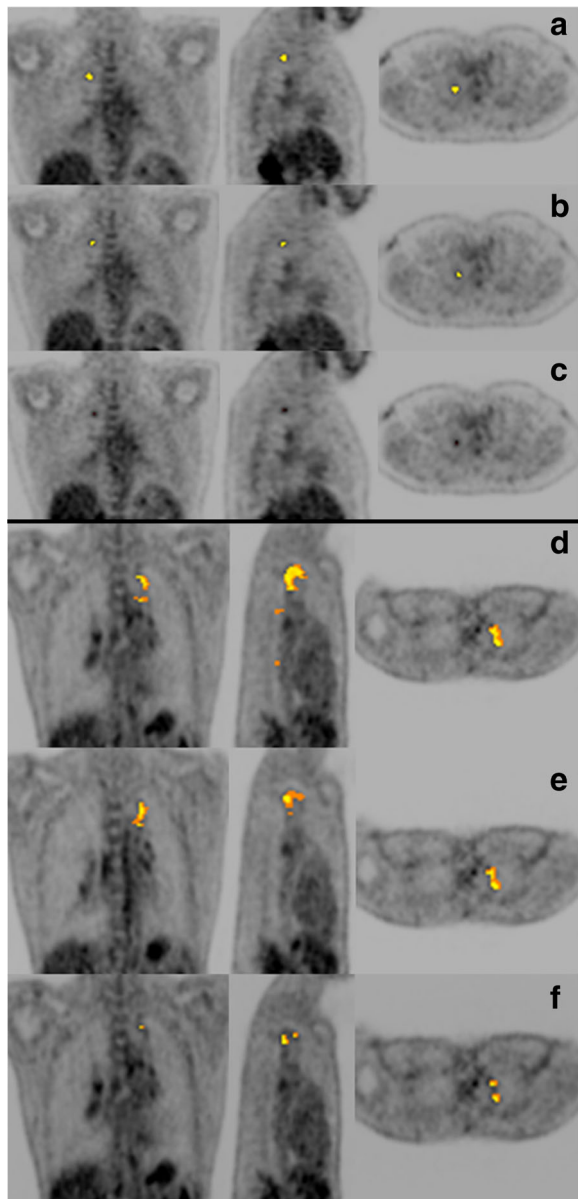


**Fig. 4** Coronal (left), sagittal (middle) and transverse views of PET scans of two patients after treatment for pulmonary tuberculosis. The first patient (**a–c**) has a residual nodule in the right upper lobe showing minimally increased FDG avidity. The second patient (**d–f**) has a complex lesion in the left upper lobe with mild FDG avidity. The auto-delineated metabolic lesion volume is overlaid using ascending Z-score thresholds, respectively at  $Z = 7$  (**a, d**),  $Z = 8$  (**b, e**) and  $Z = 9$  (**c, f**)

#### Manual segmentation

The two manual readers are clinicians, with experience in the diagnosis and treatment of pulmonary tuberculosis. They are also clinical trial investigators and trained in PET-CT evaluation for a phase 3 clinical trial that aims to use PET-CT parameters to guide TB treatment duration [28]. Manual segmentation of

FDG-avid PET lesions in PTB scans took roughly 30–90 min per scan.

#### Statistical analysis

Volumetric comparisons were performed using the dice similarity coefficient (DSC), a validated approach to measure spatial overlap [51, 52]. In addition, the true positive volume fraction (TPFV) was calculated to indicate segmentation sensitivity and one minus the false positive volume fraction (1-FPVF) to indicate specificity. Statistical analysis was performed using Statistica Version 13©. For numerical variables we report median, range and 25th and 75th percentiles to accommodate the modest sample size included in this pilot project. Agreement measures are reported using a Bland-Altman plot showing only bias and values and not confidence intervals and standard deviations. We report the correlation coefficient and  $p$  values for correlations between numerical variables.

#### Results

##### Application of technique

We successfully implemented the quantification methodology in all controls and cases. Creating the masks required knowledge of lung anatomy, while the other steps required basic computer literacy. The user input required for quantification could be divided into (1) file management (including the selection, indexing and formatting of image files) and (2) creating VOIs for lung masks, background references and areas affected by motion misregistration. The time required to quantify scans ranged approximately from 10 min for a lesion-free lung scan at one time-point, to 45 min for a three time point series of extensively diseased lungs. Where applicable, cavity volumes were easily measured with MRICro's 3D region-growing tool on CT, taking less than 1 min per scan.

The auto-segmented MLV for each scan corresponded well with visual assessment of the PET scans. No false positive segmentation was noted on control scans. In the PTB lung scans, all auto-segmented MLVs corresponded to areas that appeared FDG avid. No visually FDG-avid lesions were missed by auto-segmentation.

FDG-avid lesions were also segmented using T40%. However, when max lesion SUV decreased during treatment, the MLVs became progressively more inclusive and did not correspond well to visual assessment. As such, we abandoned T40% as a method to monitor treatment response in a whole lung VOI.

Table 2 shows a summary of DSC values (Table 2), true positive volume fraction (TPVF; Table 2), 1-false positive volume fraction (1-FPVF; Table 2), between readers and automated thresholds at Dx, M6 and combined. Individual segments corresponded better at Dx

**Table 2** Summary of comparisons between independent readers, reader A and reader B, and automated thresholding segmentations using the Z-score (Z-A and Z-B) and SUV > 1 (SUV). Values for dice similarity coefficient (DSC), true positive volume fraction (TPVF) and 1 minus false positive volume fraction (1-FPVF) are shown

	Dx and M6		Dx		M6	
	Median	Range	Median	Range	Median	Range
DSC						
Z-A to reader A	0.75	0.57–0.91	0.85	0.57–0.91	0.68	0.61–0.84
Z-A to reader B	0.66	0.31–0.94	0.77	0.56–0.94	0.55	0.31–0.79
Z-A to intersection	0.73	0.46–0.89	0.81	0.49–0.89	0.64	0.46–0.78
Z-A to union	0.72	0.30–0.94	0.81	0.63–0.94	0.55	0.30–0.85
SUV to reader A	0.68	0.21–0.90	0.74	0.57–0.90	0.47	0.21–0.77
SUV to reader B	0.63	0.19–0.91	0.75	0.57–0.91	0.45	0.19–0.71
SUV to intersection	0.61	0.11–0.88	0.74	0.50–0.88	0.45	0.11–0.69
SUV to union	0.7	0.18–0.92	0.77	0.64–0.92	0.37	0.18–0.79
Z-A to SUV	0.88	0.15–0.99	0.88	0.75–0.97	0.59	0.15–0.99
Z-B to Z-A	0.83	0.59–0.99	0.89	0.79–0.99	0.63	0.59–0.95
Reader B to A	0.78	0.42–0.92	0.83	0.78–0.92	0.64	0.42–0.85
TPVF (%)						
Z-A to reader A	91.4	55.48–100.00	98.9	89.21–100.00	78.5	55.48–93.65
Z-A to reader B	80.5	18.22–99.91	96.3	70.18–99.91	62.0	18.22–94.05
Z-A to intersection	98.0	59.56–100.00	99.9	94.35–100.00	87.5	59.56–98.56
Z-A to union	77.8	17.86–99.92	96.0	70.82–99.92	77.8	17.86–90.34
SUV to reader A	99.4	34.64–100.00	99.8	99.34–100.00	96.6	34.64–100.00
SUV to reader B	92.0	31.92–99.63	96.7	72.27–99.63	84.8	31.92–96.95
SUV to intersection	100.0	53.19–100.00	100.0	99.83–100.00	99.8	53.19–100.00
SUV to union	95.4	24.64–99.91	96.4	73.04–99.91	95.3	24.64–97.28
Z-A to SUV	91.4	17.09–100.00	87.9	59.49–100.00	97.5	17.09–100.00
Z-B to Z-A	92.7	56.35–100.00	86.9	70.80–100.00	100.0	56.35–100.00
Reader B to A	81.4	50.25–98.10	88.5	79.06–98.10	71.1	50.25–93.15
1-FPVF(%)						
Z-A to reader A	68.8	40.61–88.04	74.5	40.61–84.70	61.3	55.79–88.04
Z-A to reader B	68.3	31.79–100.00	74.4	39.29–91.24	52.9	31.79–100.00
Z-A to intersection	62.7	30.95–88.04	70.8	32.51–79.93	47.9	30.95–88.04
Z-A to union	75.7	30.54–100.00	88.3	46.25–92.29	62.2	30.54–100.00
SUV to reader A	57.7	11.82–81.57	59.2	39.99–81.57	54.4	11.82–73.02
SUV to reader B	54.6	10.97–85.55	74.6	40.51–85.55	42.8	10.97–70.14
SUV to intersection	48.6	6.10–78.25	58.2	32.94–78.25	30.2	6.10–69.07
SUV to union	66.0	9.91–88.88	75.7	46.85–88.88	55.2	9.91–74.10
Z-A to SUV	100.0	8.36–100.00	100.0	77.01–100.00	100.0	8.36–100.00
Z-B to Z-A	87.3	44.02–100.00	90.3	86.36–100.00	61.5	44.02–89.62
Reader B to A	77.3	26.93–95.40	77.7	65.93–95.40	59.1	26.93–95.32

than M6, independent of which segmentation method used. DSC between manual and Z-score segmentations (Z-A to reader A and Z-A to reader B) was slightly lower than between the manual readers (reader B to reader A), but higher than DSC between manual and SUV > 1

segmentations. The same trends were noted in regard to 1-FPVF(%) values. In contrast, SUV > 1 segments performed better in regard to TPVF comparison than either Z-score or manual segmentation. The same behaviour was also observed when comparing to either unions or

the intersections. The DSC between MLV segmented using the Z-score and the MLV intersection between the readers was 0.73 (range 0.46–0.94), while the DSC between the readers’ MLV union was 0.72 (range 0.3–0.94). The median DSC between the MLV segmented using SUV > 1 and the readers’ segments intersection was 0.61 (range 0.11–0.88) and 0.7 (range 0.18–0.92) when compared to the union of the manual segments.

Inter-user Z-score segmentation (created by different spheres and lung mask) and inter-reader manual segmentation showed similar variability at single time-points, with a median DSC of 0.83 and 0.78 respectively (Table 2). However, there was a much better agreement in percentage change from diagnosis to M6 for inter-user Z-score segmentation than for manual inter-reader segmentation. The difference between the percentage change from Dx to M6 in MLV lesions volume ranged from -3.69 to 0.96 for inter-user Z-scores and -8.44 to 21.51 for inter-reader MLV change (Fig. 5).

Z-score segmentation correlated well with SUV > 1 (median DSC = 0.88). In addition, there was a high correlation between TGA (product of  $SUV_{mean}$  and MLV in SUV > 1) and TGAI (product of mean lesion-to-background intensity and MLV in Z-score > 8) across time-points (Dx, M1, M6, Fig. 6a), which improved when assessing change in inflammatory burden over time (Fig. 6b, c).

**Response to therapy**

Representative quantification patterns of scans from a control case and PTB patients before, during, and after treatment, with an overlay of the segmented MLV and a scatterplot representing the voxels from each scan, are shown in Fig. 7. The scatter plot of a control scan is shown in Fig. 7a. The cured patients’ values (Fig. 7b, c) change toward normal at follow-up, while for the patient who failed treatment the pattern remains clearly abnormal on the density and intensity axes (Fig. 7d).

Figure 8 demonstrates the dynamics of different scan parameters during treatment of the five PTB cases, in relation to clinical outcome. The segmented TGAI (Fig. 8a) of three out of four cured cases already showed partial reduction (30–62%) at M1 and continued to decrease markedly toward the end of treatment. The fourth cured patient showed a slight increase by M1, but significant reduction by M6. After 6 months of treatment, all the cured patients showed marked reduction (80–99%), but only one patient showed nearly complete metabolic resolution. The patient that failed treatment remained unchanged over the first month and deteriorated by M6. The MLV for this patient (Fig. 8b) showed very similar patterns during treatment.

The combined lung volume with increased density ( $V_{soft} + medium + hard$ ) followed a similar trend, although

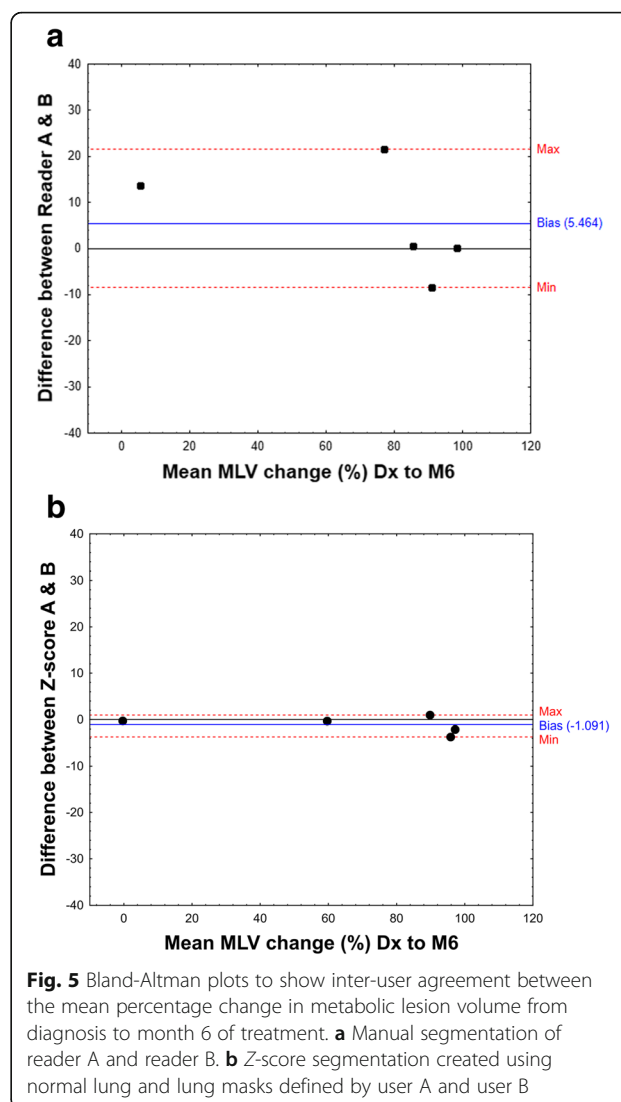
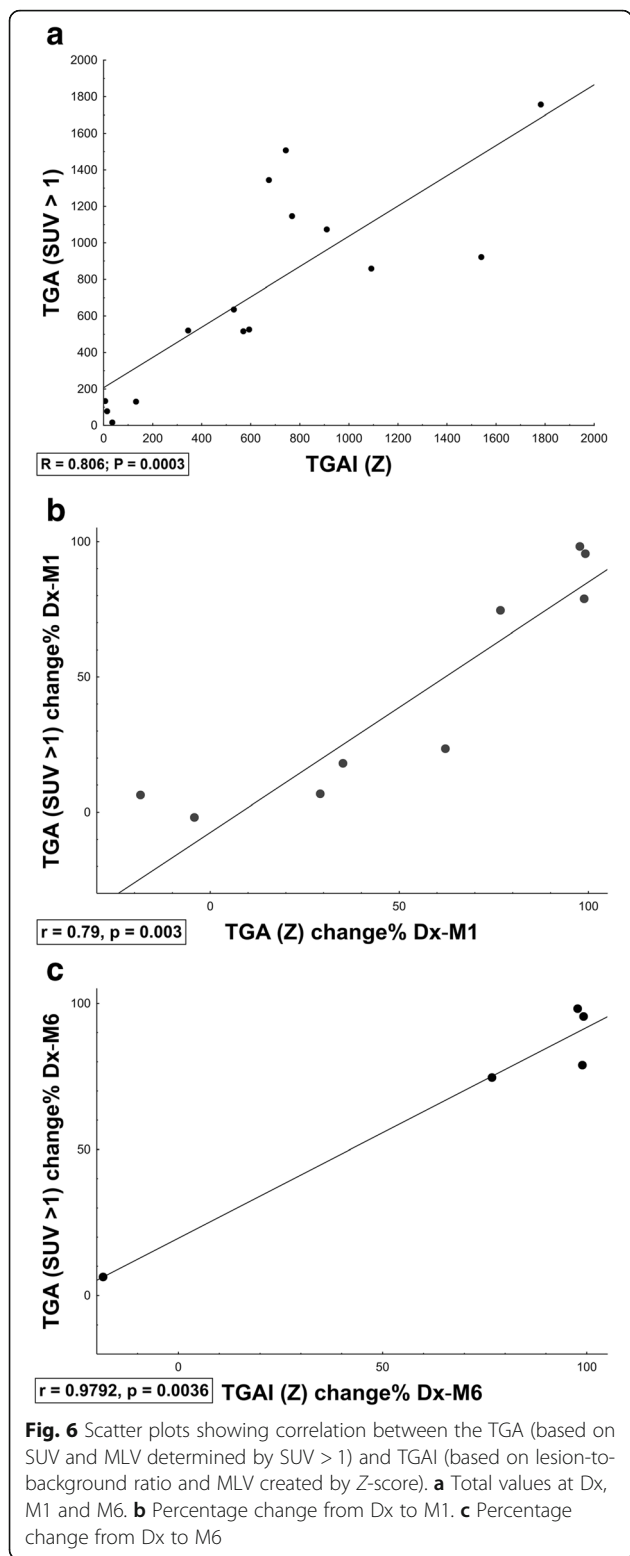


**Fig. 5** Bland-Altman plots to show inter-user agreement between the mean percentage change in metabolic lesion volume from diagnosis to month 6 of treatment. **a** Manual segmentation of reader A and reader B. **b** Z-score segmentation created using normal lung and lung masks defined by user A and user B

the decrease from Dx to M6 was less marked (41–83%) than MLV changes and the failed treatment patient showed only slightly decreased values from Dx to M6. In the breakdown of lesions of different density (Fig. 8c–e), all cured patients showed a marked volume decrease in hard lesions, already noted by M1 (35–71% reduction) and continued toward M6 (81–98% reduction). The volumes of medium and soft lesions were more variable, and a relatively large residual lesion volume was present at M6 for most cases.

After 1 month of treatment, in cured patients,  $MLV_{abn}$  (Fig. 8f) decreased modestly in two and remained stable in the other two. The failed treatment case showed a 13% increase. At M6, however, all cured cases’  $MLV_{abn}$  had decreased markedly (82–98%), while the failed treatment case showed a further increase.



**Discussion**

In this paper, we present a technique to reproducibly quantify pulmonary tuberculosis lesions on PET and CT. We used patient-specific reference volumes to reduce intra-

and interscan variability on PET and auto-delineation to reduce inter-reader and inter-user variability when assessing multiple widely distributed lesions with complex morphology. The technique quantifies lesions throughout the lungs in order to measure the central trend of disease progression or resolution, thus compensating for the variable response of individual lesions during PTB treatment.

The technique introduced some novel concepts in PET-CT analysis including the use of a patient-specific reference volume to standardise lung uptake (lesion-to-background), whole lung automated segmentation of CT lesions and bivariate quantification of PET and CT images. It also reapplies concepts previously used in other settings, such as co-registration of corresponding scans at different time-points, whole organ (semi-)automated segmentation of PET uptake, and joint segmentation of PET and CT [23].

Optimal adaptive thresholds for auto-segmentation of PET scans were determined using a set of control lung scans and scans containing lesions with minimal to mildly increased uptake. Density thresholds for CT scans were determined using values previously reported in literature [41].

We compared the Z-score delineation to manual delineation by two independent readers and a fixed threshold previously used in a TB trial (SUV > 1) [41]. There was better correlation between the Z-score and manual segmentation when compared to the fixed threshold. We also found decreased inter-user variability when measuring response to treatment when compared to manual segmentation. However, there was still some inter-user variability at single time-points, which would not apply when using a fixed threshold (SUV > 1). Both automated thresholding techniques saved time and appeared highly sensitive. We also applied a gradient-based threshold (T40%); however, it did not appear to be appropriate to measure response to treatment in whole lung VOIs. After treatment, agreement between all thresholding techniques and readers were lower than previous reports only focussing on diagnosis [6]. However, this was expected in highly complex lesions at the very edge of FDG avidity, found after treatment.

There was good correlation between TGA (based on mean SUV and volume) and TGAI (normalised to background lung activity), especially when measuring changes over time.

We tested whether the technique was accurate enough to measure changes over time, by applying it to independent pilot sets of control cases and PTB cases during treatment. The quantified variables detected marked changes within 1 month of treatment. The metrics corresponded well with visual scan interpretation, clinical outcomes and the qualitative classification allocated during analysis for the parent study. It also provided a range of additional information.

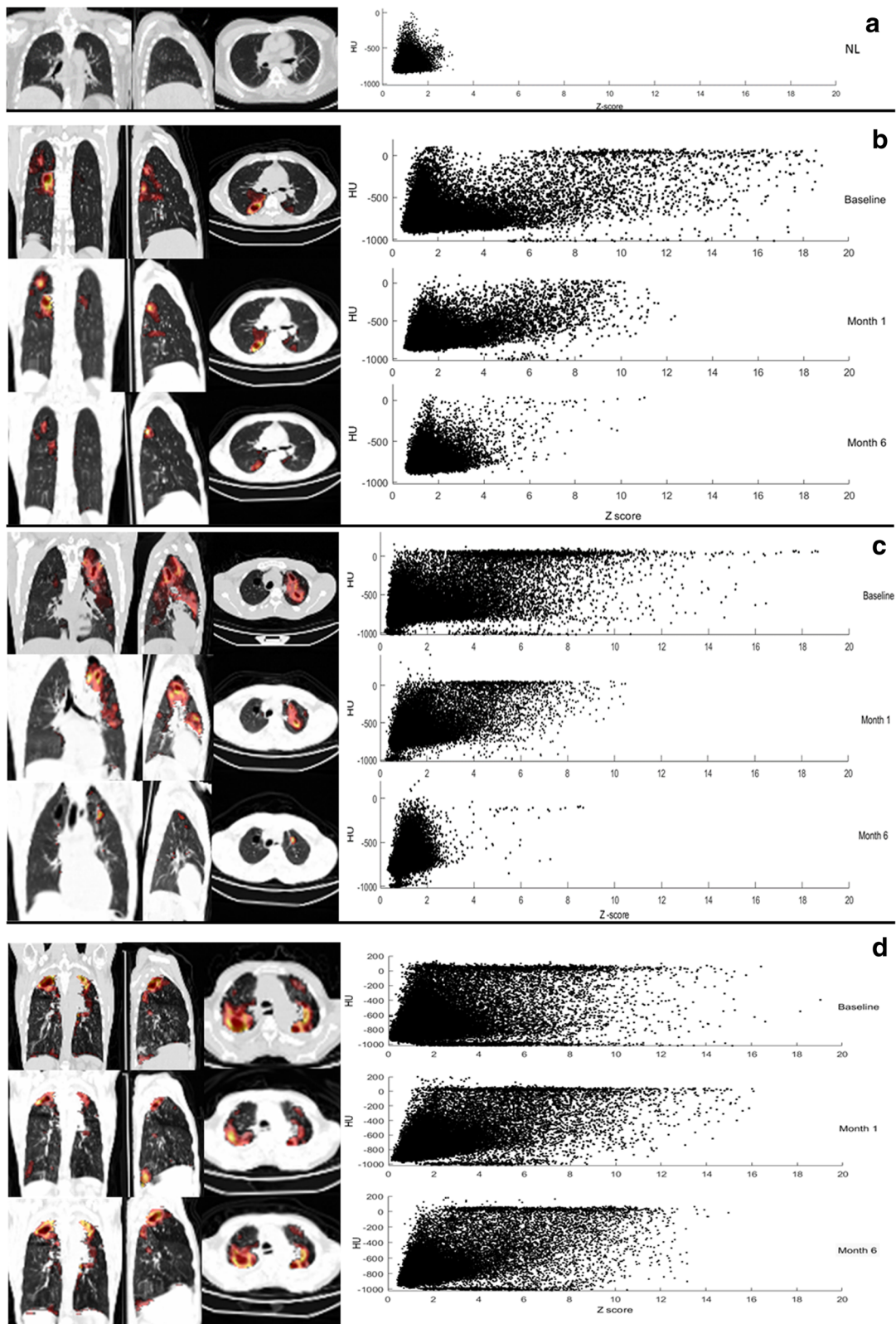


**Fig. 7** (See legend on next page.)

(See figure on previous page.)

**Fig. 7** This shows coronal (left), sagittal (middle) and transverse (right) views of different CT images with the auto-delineated metabolic lesion volume as an overlay and a scatterplot representing the CT density (Y axis, HU) and the PET uptake intensity (X axis; Z-score) of the voxels held within the lung mask **a** Lesion-free lungs from control participant. **b-d** Dx, M1 and M6 PET-CT scans for PTB patients. **b** Cured patient with an improved scan response and moderate uptake still present at M6. **c** Cured patient, with a resolved scan response. Only minimal intensity residual lesions and thin-walled cavities still present at M6. **d** Failed treatment case, with a mixed scan response pattern and multiple lesions with very high uptake present at M6

Some challenges and potential drawbacks were encountered during this pilot application. While using the 3D region-growing tool in MRIcro was user friendly and easily reproducible, some manual input was required when drawing the lung mask, to include dense lesions extending into the chest wall, and areas of motion misregistration. In the future, computer-assisted drawing tools or fully

automated lung atlas segmentation and correction of mis-registration should decrease inter-user variability and time requirements of any automated technique.

Co-registering baseline and follow-up scans allowed the user to generate a single-lung mask and reference volume to use across all time points. This reduced inter-scan variability and saved time. It did not, however, allow

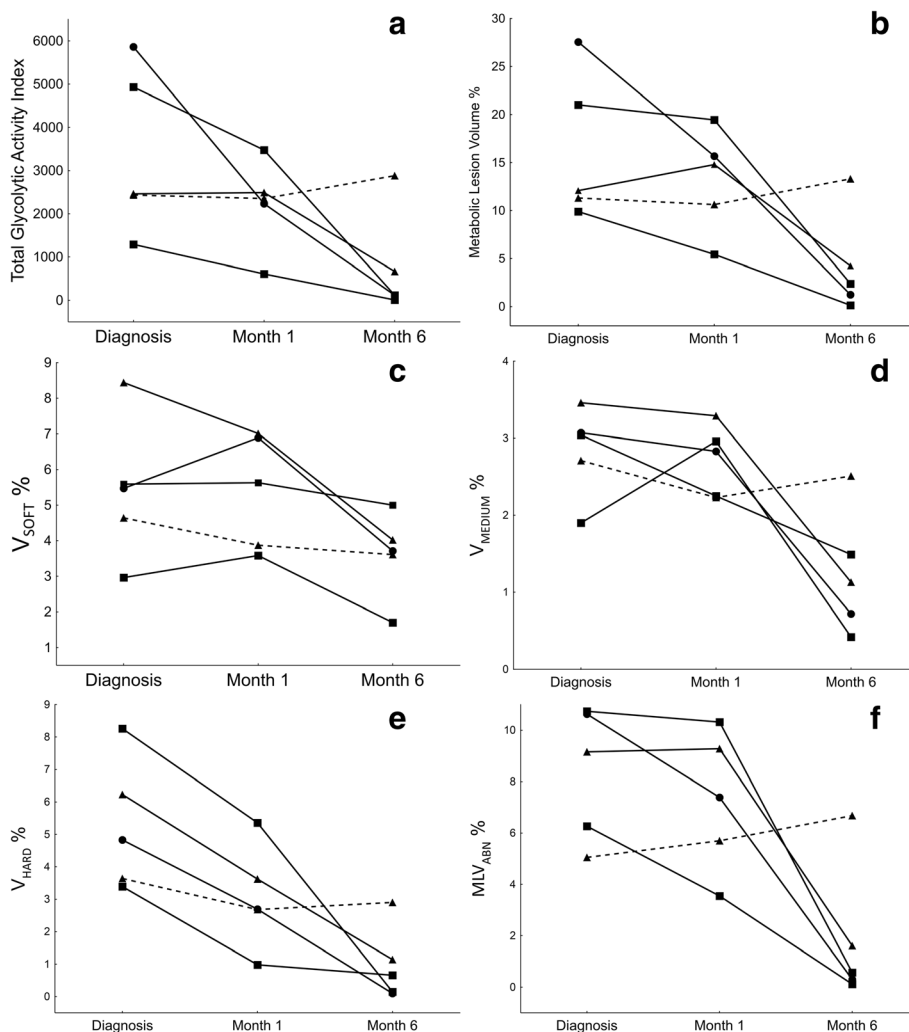


**Fig. 8** These graphs represent the case-profiles of five different PTB patients and the changes of various auto-segmented PET-CT parameters at Dx, M1 and M6 (X axis). A straight line represents a cured outcome and the broken line indicates treatment failure. **a** Total glycolytic activity index. **b** Metabolic lesion volume as a percentage of total lung volume. **c**  $V_{soft}$  (- 500 HU:- 300 HU) CT lesion volume as a percentage of total lung volume. **d**  $V_{medium}$  (- 300 HU:- 100 HU) CT lesion volume as a percentage of total lung volume. **e**  $V_{hard}$  (> - 100 HU) CT lesion volume as a percentage of total lung volume. **f** Area of lung that shows abnormal density (> - 500 HU) and relative high uptake intensity as a percentage of total lung volume

for the measurement of changes in total lung volume over time, which may occur after lesion resolution with associated fibrosis. Re-slicing allowed direct voxel comparison of PET and CT components using a single VOI. A disadvantage is that there was a smoothing effect on the CT images. Using a density threshold was not specific enough to delineate cavity volume, and an additional manual step was required to perform this function.

Using the mean and standard deviation of reference volumes to standardise lesion-to-background activity should decrease interscan and inter-patient variability compared to techniques that normalise the uptake to reference volumes from other organs or a theoretical whole body concentration. Thus, the Z-score takes into account the variability of FDG uptake in normal lung tissue and does not depend on dose or weight. The advantage of the latter is that changes in weight induce changes in SUV, while not necessarily inducing a change in FDG uptake.

Semi-automatic delineation of the whole lung allowed for segmentation of multiple lesions with widespread distribution and variable intensity, size and morphology. This shows promise to reduce inter-reader variability, especially in a self-controlled study measuring changes after interventions.

## Conclusions

This technique to auto-segment and quantify multi-focal and complex lung lesions on PET and CT images shows great promise in a pilot set of subjects and required limited operator input. This study was only a small pilot study as proof-of-concept. Validation in a larger cohort, and comparison of scan metrics to clinical outcomes and biomarkers is required to determine indicators of prognosis and cure. Ultimately this methodology, or features thereof, could be incorporated into standard clinical analysis pipelines and research protocols.

## Abbreviations

CT: Computed tomography; Dx: Diagnosis; HU: Hounsfield units; M1: Month 1; M6: Month 6; MLV: Metabolic lesion volume with high density ( $> -500$  HU); MLV<sub>abn</sub>: Metabolic lesion volume with high density ( $> -500$  HU) and high intensity ( $> Z$ -score 8); NL: Normal lung parenchyma; PET: Positron emission tomography; PTB: Pulmonary tuberculosis; TGA: Total glycolytic activity ( $SUV_{mean} \times$  lesion volume); TGAi: Total glycolytic activity index (mean lesion-to-background  $\times$  lesion volume); TLV: Total lung volume; V<sub>hard</sub>: Hard lesion volume ( $> -100$  HU); V<sub>low</sub>: Hypodense lesion volume ( $> -950$  HU); V<sub>medium</sub>: Medium lesion volume ( $-300$  HU to  $-100$  HU); VOI: Volume of interest; V<sub>soft</sub>: Soft lesion volume ( $-500$  HU to  $-300$  HU); Z: Z-score/standardised score; Z<sub>mean</sub>: Mean standardised intensity

## Acknowledgements

We thank our participants for their willingness to take part in this study. Further, we acknowledge the staff at the Stellenbosch University Immunology Research Group, the Western Cape Academic PET-CT Centre, Ithemba LABS, and Tygerberg Academic Hospital's Nuclear Medicine

Department and Pulmonology Unit, as well as the managers and health care providers from the City of Cape Town Health Department.

The Catalysis Biomarker Consortium: Stephanus T. Malherbe<sup>1,2</sup>, Patrick Dupont<sup>3,4</sup>, Ilse Kant<sup>4</sup>, Katharina Ronacher<sup>1,2</sup>, Magdalena Kriel<sup>1,2</sup>, André G. Loxton<sup>1,2</sup>, Ray Y. Chen<sup>5</sup>, Laura E. Via<sup>5,6</sup>, Friedrich Thienemann<sup>6,7</sup>, Robert J. Wilkinson<sup>6,7,8,9</sup>, Clifton E. Barry III<sup>1,2,5,6</sup>, Stephanie Griffith-Richards<sup>10</sup>, Annare Ellman<sup>4</sup>, Jill Winter<sup>11</sup>, Gerhard Walzl<sup>1,2</sup>, Nelita Du Plessis<sup>1,2</sup>, Caroline G.G. Beltran<sup>1,2</sup>, Lani Thiar<sup>1,2</sup>, Gerard Tromp<sup>1,2</sup>, Lance A. Lucas<sup>1,2</sup>, Bronwyn Smith<sup>1,2</sup>, Kim Stanley<sup>1,2</sup>, David Alland<sup>1,2</sup>, Shubhada Shenai<sup>1,2</sup>, Lori E. Dodd<sup>1,3</sup>, and James M. Warwick<sup>4</sup>.

1. Department of Science and Technology/National Research Foundation Centre of Excellence for Biomedical Tuberculosis Research and South African Medical Research Council Centre for Tuberculosis Research.
2. Division of Molecular Biology and Human Genetics, Faculty of Medicine and Health Sciences, Stellenbosch University, Cape Town, South Africa.
3. Laboratory for Cognitive Neurology, Department of Neurosciences, KU Leuven, Belgium.
4. Division of Nuclear Medicine, Department of Medical Imaging and Clinical Oncology, Faculty of Medicine and Health Sciences, Stellenbosch University, Cape Town, South Africa.
5. Tuberculosis Research Section, Laboratory of Clinical Infectious Diseases, Division of Intramural Research, National Institute of Allergy and Infectious Diseases, National Institutes of Health, Bethesda, MD, USA.
6. Wellcome Centre for Infectious Diseases Research in Africa, Institute of Infectious Disease and Molecular Medicine, Faculty of Health Science, University of Cape Town, Observatory 7925, Republic of South Africa
7. Department of Medicine, Groote Schuur Hospital, Faculty of Health Science, University of Cape Town, Cape Town, South Africa.
8. The Francis Crick Institute, Midland Road, London NW1 2AT, UK
9. Department of Medicine, Imperial College London W2 1PG, UK
10. Division of Radiodiagnosis, Department of Medical Imaging and Clinical Oncology, Faculty of Medicine and Health Sciences, Stellenbosch University, Cape Town, South Africa.
11. Catalysis Foundation for Health, Emeryville, CA, USA.
12. Center for Emerging Pathogens, Department of Medicine, Rutgers-New Jersey Medical School, Rutgers Biomedical and Health Sciences, Newark, NJ, USA.
13. Biostatistics Research Branch, National Institute of Allergy and Infectious Diseases, National Institutes of Health Bethesda, Maryland, USA.

## Funding

Funding was provided by the Catalysis Foundation for Health, the Division of Intramural Research, National Institute of Allergy and Infectious Diseases, the South African National Research Fund and the South African Medical Research Council's Clinician Scholarship Program, as well as the National Institute of Allergy and Infectious Diseases, International Collaborations in Infectious Disease Research. RJW is supported by the Francis Crick Institute, which receives its core funding from Cancer Research UK (FC00110218), the UK Medical Research Council (FC00110218) and the Wellcome Trust (FC00110218). He also receives support from the Wellcome Trust (104803 and 203135) and the South African MRC Strategic Health Innovations Partnership. STM receives funding from the EDCTP2 programme supported by the European Union (grant number CDF1576). The views and opinions of the authors expressed herein do not necessarily state or reflect those of the EDCTP.

## Availability of data and materials

Datasets would be made available on request to the author.

## Authors' contributions

STM managed the patient recruitment, follow-up and sample collection; assisted in the programming; optimised the technique; performed the visual scan analysis; implemented the analysis and drafted the manuscript. JMWW, IK and PD designed the technique, created the program, analysed the results and edited the manuscript. AGL, KR, LEV, CEB, JW, RYC and GW designed the study, analysed the results and edited the manuscript. MK, FT and RJW were

involved in study design, patient recruitment and edited the manuscript. PA, AE and SG-R performed the visual scan analysis and edited the manuscript. All authors reviewed and agreed to the manuscript content.

#### Ethics approval and consent to participate

Ethical approval was obtained for all study-related activities from the Stellenbosch University Human Research Ethics Committee (reference numbers N10/01/013 and N14/10/155). All participants signed the informed consent.

#### Consent for publication

This manuscript does not contain any personal sensitive data and is therefore not applicable.

#### Competing interests

The authors declare that they have no competing interests.

#### Author details

<sup>1</sup>DDST-NRF Centre of Excellence for Biomedical Tuberculosis Research and South African Medical Research Council Centre for Tuberculosis Research, Cape Town, South Africa. <sup>2</sup>Division of Molecular Biology and Human Genetics, Faculty of Medicine and Health Sciences, Stellenbosch University, Cape Town, South Africa. <sup>3</sup>Department of Neurosciences, Laboratory for Cognitive Neurology, KU Leuven, Belgium. <sup>4</sup>Division of Nuclear Medicine, Department of Medical Imaging and Clinical Oncology, Faculty of Medicine and Health Sciences, Stellenbosch University, Cape Town, South Africa. <sup>5</sup>Tuberculosis Research Section, Laboratory of Clinical Infectious Diseases, Division of Intramural Research, National Institute of Allergy and Infectious Diseases, National Institutes of Health, Bethesda, MD, USA. <sup>6</sup>Wellcome Centre for Infectious Disease Research in Africa, Institute of Infectious Disease and Molecular Medicine, Faculty of Health Science, University of Cape Town, Observatory 7925, Republic of South Africa. <sup>7</sup>Department of Medicine, Faculty of Health Science, Groote Schuur Hospital, University of Cape Town, Cape Town, South Africa. <sup>8</sup>The Francis Crick Institute, Midland Road, London NW1 2AT, UK. <sup>9</sup>Department of Medicine, Imperial College London, London W2 1PG, UK. <sup>10</sup>Division of Radiodiagnosis, Department of Medical Imaging and Clinical Oncology, Faculty of Medicine and Health Sciences, Stellenbosch University, Cape Town, South Africa. <sup>11</sup>Translational Research Institute, Mater Research Institute – The University of Queensland, Brisbane, QLD, Australia. <sup>12</sup>Catalysis Foundation for Health, Emeryville, CA, USA.

Received: 5 April 2018 Accepted: 8 June 2018

Published online: 25 June 2018

#### References

- Maldonado A, González-Alenda FJ, Alonso M, Sierra JM. PET-CT in clinical oncology. *Clin Transl Oncol*. 2007;9(8):494–505.
- Hess S, Hansson SH, Pedersen KT, Basu S, Høiland-Carlsen PF. FDG-PET/CT in infectious and inflammatory diseases. *PET Clin*. 2014;9(4):497–519.
- Cheebsumon P, van Velden FHP, Yaqub M, Frings V, de Langen AJ, Hoekstra OS, et al. Effects of image characteristics on performance of tumor delineation methods: a test-retest assessment. *J Nucl Med*. 2011;52(10):1550–8.
- Huang W, Zhou T, Ma L, Sun H, Gong H, Wang J, et al. Standard uptake value and metabolic tumor volume of <sup>18</sup>F-FDG PET/CT predict short-term outcome early in the course of chemoradiotherapy in advanced non-small cell lung cancer. *Eur J Nucl Med Mol Imaging*. 2011;38(9):1628–35.
- Dibble EH, Alvarez ACL, Truong M-T, Mercier G, Cook EF, Subramaniam RM. 18F-FDG metabolic tumor volume and total glycolytic activity of oral cavity and oropharyngeal squamous cell cancer: adding value to clinical staging. *J Nucl Med*. 2012;53(5):709–15.
- Foster B, Bagci U, Mansoor A, Xu Z, Mollura DJ. A review on segmentation of positron emission tomography images. *Comput Biol Med*. 2014;50:76–96.
- Fletcher JW. PET/CT standardized uptake values (SUVs) in clinical practice assessing response to therapy. *Semin Ultrasound CT MRI*. 2010;31(6):496–505.
- Lowe VJ, Hoffman JM, DeLong DM, Patz EF, Coleman RE. Semiquantitative and visual analysis of FDG-PET images in pulmonary abnormalities. *J Nucl Med*. 1994;35(11):1771–6.
- Hatt M, Cheze-Le Rest C, Aboagye EO, Kenny LM, Rosso L, Turkheimer FE, et al. Reproducibility of 18F-FDG and 3'-deoxy-3'-18F-fluorothymidine PET tumor volume measurements. *J Nucl Med*. 2010;51(9):1368–76.
- Boellaard R, O'Doherty MJ, Weber WA, Mottaghy FM, Lonsdale MN, Stroobants SG, et al. FDG PET and PET/CT: EANM procedure guidelines for tumour PET imaging: version 1.0. *Eur J Nucl Med Mol Imaging*. 2010;37(1):181–200.
- Fogh SE, Bs JK, Bs AF, Intenzo C, Axelrod R, Mccue P, et al. Pathological correlation of PET/CT based auto contouring for radiation planning of lung cancer. *Bodine J*. 2010;78(3):202–3.
- Dann EJ, Bar-Shalom R, Tamir A, Epelbaum R, Avivi I, Ben-Shachar M, et al. A functional dynamic scoring model to elucidate the significance of post-induction interim fluorine-18-fluorodeoxyglucose positron emission tomography findings in patients with Hodgkin's lymphoma. *Haematologica*. 2010;95:1198–206.
- Delbeke D, Stroobants S, de Kerviler E, Gisselbrecht C, Meignan M, Conti PS. Expert opinions on positron emission tomography and computed tomography imaging in lymphoma. *Oncologist*. 2009;14(Suppl 2):30–40.
- Firouzian A, Kelly MD, Declerck JM. Insight on automated lesion delineation methods for PET data. *EJNMMI Res*. 2014;4(1):1–12.
- Boellaard R, Krak NC, Hoekstra OS, Lammertsma AA. Effects of noise, image resolution, and ROI definition on the accuracy of standard uptake values: a simulation study. *J Nucl Med*. 2004;45(9):1519–27.
- Chien D, Lodge M, Wahl R. Reproducibility of liver and mediastinal blood pool F-18 activity as normal reference tissues. *J Nucl Med*. 2011;52:536. abstract
- Higashi K, Ito K, Hiramatsu Y, Ishikawa T, Sakuma T, Matsunari I, et al. 18F-FDG uptake by primary tumor as a predictor of intratumoral lymphatic vessel invasion and lymph node involvement in non-small cell lung cancer: analysis of a multicenter study. *J Nucl Med*. 2005;46(2):267–73.
- Barrington SF, Qian W, Somer EJ, Franceschetto A, Bagni B, Brun E, et al. Concordance between four European centres of PET reporting criteria designed for use in multicentre trials in Hodgkin lymphoma. *Eur J Nucl Med Mol Imaging*. 2010;37(10):1824–33.
- Chong D, Brown MS, Kim HJ, van Rikxoort EM, Guzman L, McNitt-Gray MF, et al. Reproducibility of volume and densitometric measures of emphysema on repeat computed tomography with an interval of 1 week. *Eur Radiol*. 2012;22(2):287–94.
- Colombi D, Dinkel J, Weinheimer O, Obermayer B, Buzan T, Nabers D, et al. Visual vs fully automatic histogram-based assessment of idiopathic pulmonary fibrosis (IPF) progression using sequential multidetector computed tomography (MDCT). *PLoS One*. 2015;10(6):e0130653.
- Karimi R, Tornling G, Forsslund H. Lung density on high resolution computer tomography (HRCT) reflects degree of inflammation in smokers. *Respir Res*. 2014;15(23):1–10.
- Shin KE, Chung MJ, Jung MP, Choe BK, Lee KS. Quantitative computed tomographic indexes in diffuse interstitial lung disease: correlation with physiologic tests and computed tomography visual scores. *J Comput Assist Tomogr*. 2011;35(2):266–71.
- Bagci U, Udupa JK, Mendhiratta N, Foster B, Xu Z, Yao J, Chen X, Mollura DJ. Joint segmentation of anatomical and functional images: applications in quantification of lesions from PET, PET-CT, MRI-PET, and MRI-PET-CT images. *Med Image Anal*. 2013;17(8):929–45.
- Hu Y, Mangan JA, Dhillon J, Sole KM, Mitchison DA, Butcher PD, et al. Detection of mRNA transcripts and active transcription in persistent Mycobacterium tuberculosis induced by exposure to rifampin or pyrazinamide. *J Bacteriol*. 2000;182(22):6358–65.
- Boshoff HI, Barry CE 3rd. Tuberculosis—metabolism and respiration in the absence of growth. *Nat Rev Microbiol*. 2005;3(1):70–80.
- Mitchison DA. Basic mechanisms of chemotherapy. *Chest*. 1979;76(6):771–6, 778–81.
- Johnson DH, Via LE, Kim P, Laddy D, Lau CY, Weinstein EA, et al. Nuclear imaging: a powerful novel approach for tuberculosis. *Nucl Med Biol*. 2014;41(10):777–84.
- Chen RY, Via LE, Dodd LE, Walz G, Malherbe ST, Loxton AG, et al. Using biomarkers to predict TB treatment duration (predict TB): a prospective, randomized, noninferiority, treatment shortening clinical trial. *Gates Open Res*. 2017;1:9.
- Sathegke MM, Ankras AO, Lawal I, Vorster M. Monitoring response to therapy. *Semin Nucl Med*. 2018;48(2):166–81.
- Lin PL, Coleman T, Carney JJP, Lopresti BJ, Tomko J, Fillmore D, et al. Radiologic responses in cynomolgus macaques for assessing tuberculosis chemotherapy regimens. *Antimicrob Agents Chemother*. 2013;57(9):4237–44.
- Chen RY, Dodd LE, Lee M, Paripati P, D a H, Mountz JM, et al. PET/CT imaging reveals a therapeutic response to oxazolidinones in macaques and humans with tuberculosis. *Sci Transl Med*. 2014;6(265):265ra167.
- Via LE, Schimel D, Weiner DM, Dartois V, Dayao E, Cai Y, et al. Infection dynamics and response to chemotherapy in a rabbit model of tuberculosis

- using [<sup>18</sup>F]2-fluoro-deoxy-D-glucose positron emission tomography and computed tomography. *Antimicrob Agents Chemother.* 2012;56(8):4391–402.
33. Lin PL, Ford CB, Coleman MT, Myers AJ, Joerger T, Sacchetti J, et al. Sterilization of granulomas is common in both active and latent tuberculosis despite extensive within-host variability in bacterial killing. *Nat Med.* 2014;20(1):75–9.
  34. Davis SL, Nuernberger EL, Um PK, Vidal C, Jedynak B, Pomper MG, et al. Noninvasive pulmonary [<sup>18</sup>F]-2-fluoro-deoxy-D-glucose positron emission tomography correlates with bactericidal activity of tuberculosis drug treatment. *Antimicrob Agents Chemother.* 2009;53(11):4879–84.
  35. Mattila JT, Beaino W, Maiello P, Coleman MT, White AG, Scanga CA, et al. Positron emission tomography imaging of macaques with tuberculosis identifies temporal changes in granuloma glucose metabolism and integrin α4β1-expressing immune cells. *J Immunol.* 2017;199(2):806–15.
  36. Martinez V, Castilla-Lievre MA, Guillet-Caruba C, Grenier G, Fior R, Desarnaud S, et al. (18)F-FDG PET/CT in tuberculosis: an early non-invasive marker of therapeutic response. *Int J Tuberc Lung Dis.* 2012;16(9):1180–5.
  37. Dureja S, Sen I, Acharya S. Potential role of F18 FDG PET-CT as an imaging biomarker for the noninvasive evaluation in uncomplicated skeletal tuberculosis: a prospective clinical observational. *Eur Spine J.* 2014;23(11):2449–54.
  38. Demura Y, Tsuchida T, Uesaka D, Umeda Y, Morikawa M, Ameshima S, et al. Usefulness of (18)F-fluorodeoxyglucose positron emission tomography for diagnosing disease activity and monitoring therapeutic response in patients with pulmonary mycobacteriosis. *Eur J Nucl Med Mol Imaging.* 2009;36(4):632–9.
  39. Sathekege M, Maes A, Kgomomo M, Stoltz A, Van de Wiele C. Use of 18F-FDG PET to predict response to first-line tuberculostatics in HIV-associated tuberculosis. *J Nucl Med.* 2011;52(6):880–5.
  40. Jehanno N, Cassou-Mounat T, Vincent-Salomon A, Luporsi M, Bedoui M, Kuhnowski F. PET/CT imaging in management of concomitant Hodgkin lymphoma and tuberculosis—a problem solver tool. *Clin Case Reports.* 2018;6(1):232–4.
  41. Chen RY, Dodd LE, Lee M, Paripati P, Hammoud DA, Mountz JM, et al. PET/CT imaging correlates with treatment outcome in patients with multidrug-resistant tuberculosis. *Sci Transl Med.* 2014;6(265):265ra166.
  42. Malherbe ST, Shenai S, Ronacher K, Loxton AG, Dolganov G, Kriel M, et al. Persisting positron emission tomography lesion activity and Mycobacterium tuberculosis mRNA after tuberculosis cure. *Nat Med.* 2016;22(10):1094–100.
  43. Foster\* B, Bagci U, Xu Z, Dey B, Luna B, Bishai WR, et al. Segmentation of PET images for computer aided functional quantification of tuberculosis in small animal models. *IEEE Trans Biomed Eng.* 2014;61(3):711–24.
  44. Bagci U, Foster B, Miller-Jaster K, Luna B, Dey B, Bishai WR, et al. A computational pipeline for quantification of pulmonary infections in small animal models using serial PET-CT imaging. *EJNMMI Res.* 2013;3(1):1–41.
  45. Boellaard R, Delgado-Bolton R, Oyen WJG, Giammarile F, Tatsch K, Eschner W, et al. FDG PET / CT : EANM procedure guidelines for tumour imaging: version 2.0. *Eur J Nucl Med Mol Imaging.* 2015;42:328–54.
  46. Larobina M, Murino L. Medical image file formats. *J Digit Imaging.* 2014; 27(2):200–6.
  47. Lewis Center for Neuroimaging. MRIConvert and mcverter [Internet]. Available from: <https://lcn.uoregon.edu/downloads/mriconvert/mriconvert-and-mcverter>
  48. Welcome Trust Centre for Neuroimaging. Statistical Parametric Mapping [Internet]. Available from: <http://www.fil.ion.ucl.ac.uk/spm/>
  49. Chris Rorden. MRICro [Internet]. p. <http://people.cas.sc.edu/rorden/micro/index.html>. Available from: <http://people.cas.sc.edu/rorden/micro/index.html>
  50. Rasband W. ImageJ. <http://imagej.net>.
  51. Dice L. Measures of the amount of ecologic association between species. *Ecology.* 1945;26:297–302.
  52. Zou KH, Warfield SK, Bharatha A, Tempany CMC, Kaus MR, Haker SJ, et al. Statistical validation of image segmentation quality based on a spatial overlap index. *Acad Radiol.* 2004;11(2):178–89.

**Submit your manuscript to a SpringerOpen® journal and benefit from:**

- Convenient online submission
- Rigorous peer review
- Open access: articles freely available online
- High visibility within the field
- Retaining the copyright to your article

---

Submit your next manuscript at ► [springeropen.com](http://springeropen.com)

---